remote sensing

MDPI

Technical Note

A New Electrical Resistivity Tomography Scheme of Borehole-to-Surface-to-Cliff Detection and Imaging for Grotto Rock Structure

Jiahe Yan [1], Zhaofa Zeng [1,*], Xueyu Zhao [2], Baizhou An [1,3], Lige Bai [1], Jianwei Zhao [1] and Jing Li [1]

[1] College of Geo-Exploration Science and Technology, Jilin University, 938 Ximinzhu Street, Changchun 130026, China
[2] School of Biological, Earth and Environmental Sciences, UNSW Australia, Kensington, NSW 2052, Australia
[3] Ningxia Geophysical and Geochemical Exploration Institute (Autonomous Regional Deep Earth Exploration Center), Yinchuan 750001, China
* Correspondence: zengzf@jlu.edu.cn

Abstract: Grotto rock structure detection is precondition of the grotto protection and restoration. As a stable and non-destructive geophysical method, electrical resistivity tomography (ERT) is extensively used to detect the geological structure of the grottoes. However, the traditional ERT measurement scheme is challenging to satisfy the requirements of high accuracy and high resolution in the cliff region. Therefore, we propose a new borehole-to-surface-to-cliff ERT (BSC-ERT) scheme for grotto detection. The sensitivity patterns of five ERT schemes using three configurations (A-MN array, AB-MN array, and AM-BN array) are tested to show the detection capability of different configurations. Two numerical experiments show that the combination of borehole-to-surface ERT (BS-ERT) and surface-to-cliff ERT (SC-ERT) schemes using AM-BN array have better imaging effects and a more reasonable detection range, which is recommended to be implemented for future work. In addition, the numerical experiment also proves that the symmetric effect generated in the AM-BN array in BS-ERT scheme can be suppressed with the combination of the SC-ERT scheme.

Keywords: electrical resistivity tomography; grotto structure detection; borehole-to-surface-to-cliff ERT scheme; symmetric effect; ERT configuration

Citation: Yan, J.; Zeng, Z.; Zhao, X.; An, B.; Bai, L.; Zhao, J.; Li, J. A New Electrical Resistivity Tomography Scheme of Borehole-to-Surface-to-Cliff Detection and Imaging for Grotto Rock Structure. *Remote Sens.* **2023**, *15*, 311. https://doi.org/10.3390/rs15020311

Academic Editors: Rosa Lasaponara, Ilaria Catapano, Luca Piroddi, Sebastiano D'Amico, Marilena Cozzolino, Nasser Abu Zeid, Patrizia Capizzi and Sergio Vincenzo Calcina

Received: 29 November 2022
Revised: 30 December 2022
Accepted: 30 December 2022
Published: 5 January 2023

1. Introduction

A grotto is a kind of stone cultural relic and is usually carved into the steep sandstone cliff. It has excellent value for studying religion, history, and culture. At present, there are still a large number of grottoes preserved around the world. However, most of them face some geological degradation influenced by the nature environments. For instance, crisscross fractures formed in grottoes could lead to rock structure instability and water seepage, which is hard to solve completely due to the complex geological conditions [1–3]. In recent years, Wang et al. [4] presented a protection system to guide the protection and reinforcement of grottoes all over the world. The system shows that the evaluation of geological conditions and diseases in the cliff is the prerequisite for the further protection. Therefore, there is a need to illuminate the interior rock structure of the grottoes for grotto protection.

Geophysics methods have been widely used in archaeology and related protection. For example, surface nuclear magnetic resonance (SNMR) and spontaneous potential (SP) were used to study the origin of water seepage in JinDeng Temple grottoes and prove that the seepage mainly comes from a water-bearing area [5]. Wang [6] applied ground penetrating radar (GPR) to detect the delamination in wall paintings in Tibet and found the delamination is serious.

Electrical resistivity tomography (ERT) is also a non-destructive detection method to detect the structure by imaging underground resistivity distribution [7,8]. Three common

measurement schemes, i.e., surface, borehole-to-surface ERT (BS-ERT), and cross-hole ERT (CH-ERT), have been used along with different configurations. For example, for the surface scheme, there are the Pole-Dipole array, Dipole-Dipole array, gradient array, Schlumberger array, and full-range gradient for the ground 2D resistivity imaging, but with limited detection depth [9,10]. The other two schemes could overcome this problem and image the deep structure under the use of the borehole electrodes [11,12]. However, there are some considerations for these two schemes in terms of configuration selection. For the BS-ERT scheme, a symmetric effect is generated in some high-resolution configuration and at least two types of configurations are suggested to be used to evaluate and empress symmetric effect [13]. For CH-ERT scheme, ratio of the well distance and well depth is usually less than 0.75 to ensure the resolution and the combined configurations are necessary to improve the imaging quality [14,15].

In recent years, surface ERT scheme has been widely used in many fields, such as hydrology, archaeology, landslide, and engineering [16–19]. It has made great contributions to the exploration of the shallow region. BS-ERT scheme and CH-ERT scheme are used in place of the surface ERT scheme to detect the region beyond the detection depth of the surface ERT scheme [20–22]. Surface ERT and BS-ERT schemes have also been applied in grotto structure detection successfully. Huang et al. [23] and Fang et al. [24] used these two schemes to distinguish the fracture zone and achieved some positive results. BS-ERT scheme was measured to explore the interior resistivity structure of Mogao Grottoes [25]. Sun et al. [26] used a surface ERT scheme to investigate the moisture distribution for Mogao Grottoes as well. In addition, the timelapse surface ERT scheme is also adopted to study the current rainfall infiltration. For example, Liu et al. [27] proved that salt damage at Mogao Grottoes was greatly influenced by the rainwater infiltration, while Mao et al. [28] indicated that rainfall was not the primary source of the water seepage at Yungang Grottoes. However, some challenges still need to be solved using traditional ERT schemes. The grottoes are mainly located on the steep cliff. The region between the top surface and cliff is mainly focused and needs to be detected. The electrode spatial distribution of the traditional surface ERT scheme and BS-ERT scheme cannot meet the requirements of the high-accurate detection of the key region mentioned above. Furthermore, for the BS-ERT scheme, symmetric artifacts are easily generated when using a high-resolution AM-BN array [13], which would affect the quality of the image. Therefore, a new ERT scheme is required to be proposed for grotto structure detection.

For the grotto structure detection and protection in the near future, in this paper, we proposed a new ERT scheme for grotto structure detection called borehole-to-surface-to-cliff ERT (BSC-ERT) scheme, which was based on the BS-ERT scheme but with more cliff electrodes. Our research is mainly focused on the measurement of the BSC-ERT scheme, and an open-source software ResIPy [29] is used to implement all the numerical simulations and inversions. Three configurations (A-MN array, AB-MN array, and AM-BN array) are selected to analysis the sensitivity distribution for five single ERT schemes (surface ERT scheme, BS-ERT scheme, borehole-to-cliff ERT [BC-ERT] scheme, surface-to-cliff ERT [SC-ERT] scheme, and cliff ERT scheme) and compared with traditional ERT schemes. After that, the block model is used to study the imaging effect of five single ERT schemes and their combined schemes. At last, in order to examine the capability of the BSC-ERT scheme to detect small-scale structures and find the best combined scheme containing the least schemes, the model with water seepage structure is used in this research.

2. Methodology

2.1. 2.5-D ERT Simulation

The 2.5-D ERT assumes that the strike direction of the 3-D resistivity model is along Y-axis, and the point current electrode is used to form 3-D current flow. 2.5-D boundary-value problem converted from the 3-D partial differential equation by Fourier transform is [30]

$$\begin{cases} \nabla\cdot\left(\sigma\nabla\widetilde{V}_k\right) - k^2\sigma\widetilde{V}_k = -I\delta(x-x_0)\delta(z-z_0) & \in \Omega \\ \frac{\partial\widetilde{V}_k}{\partial n} = 0 & \in \Gamma_s \\ \frac{\partial\widetilde{V}_k}{\partial n} + \widetilde{V}_k k cos\theta\frac{\boldsymbol{K}_1(kr)}{\boldsymbol{K}_0(kr)} = 0 & \in \Gamma_\infty \end{cases} \tag{1}$$

where k is the wavenumber; δ represents the Dirac function and I is current flow at position (x_0, z_0); σ is the model conductivity distribution in area Ω; Γ_s and Γ_∞ denote surface boundary and truncated boundary, respectively; r is the distance between the position of the supply electrode and point on truncated boundary Γ_∞; $\boldsymbol{K}_0$ and $\boldsymbol{K}_1$ respectively present zero-order and first-order modified Bessel function of the second kind; $\widetilde{V}_k(x,z)$ is potential in the Fourier transform domain of wavenumber k.

Due to the unique structure of grottoes, the finite element method is recommended to solve the boundary-value problem of Equation (1) because it is easier and more flexible to discrete the mesh with complex topography. Convert Equation (1) to the equivalent variational problem:

$$\begin{cases} F\left(\widetilde{V}_k\right) = \int_\Omega \left[\frac{\sigma}{2}\left(\nabla\widetilde{V}_k\right)^2 + \frac{1}{2}k^2\sigma\widetilde{V}_k{}^2 - I\delta(A)\widetilde{V}_k\right]d\Omega + \frac{1}{2}\int_{\Gamma_\infty} k\sigma\frac{\boldsymbol{K}_1(kr)}{\boldsymbol{K}_0(kr)}\cos(r,n)\widetilde{V}_k{}^2 d\Gamma \\ \delta F\left(\widetilde{V}_k\right) = 0 \end{cases} \tag{2}$$

where $\delta(A)$ equals to $\delta(x-x_0)\delta(z-z_0)$. Solutions for variational Equation (2) can be obtained by solving the following Equation:

$$\boldsymbol{A}\boldsymbol{x} = \boldsymbol{b} \tag{3}$$

where $\boldsymbol{A}$ is the global stiffness matrix associated with the triangle mesh and resistivity model; $\boldsymbol{x}$ is a column vector storing the $\widetilde{V}_k(x,z)$; $\boldsymbol{b}$ is the matrix containing the information about the current flow. $\widetilde{V}_k(x,z)$ at each node can be calculated by solving Equation (3) and needed to be taken Fourier transform to get the potential $V(x,z)$ in spatial domain by

$$V(x,z) \approx \sum_{j=1}^{N} g_j \widetilde{V}_{k_j}(x,z) \tag{4}$$

where g_j and k_j respectively denote the weight and wavenumber of jth wavenumber; N is the number of the wavenumber k;. The choice of weight g_j and the wavenumber k_j in Equation (4) is the key to make sure the accuracy of 2.5-D ERT simulation. An optimization is used to calculate the wavenumbers and weights [31]. A combination of Gaussian quadrature and Laguerre integration can also be used to calculate the weights and wavenumbers [32,33].

2.2. Gauss-Newton Inversion

ERT inversion algorithm is an optimization which can get the model resistivity distribution through apparent resistivity or measured resistance. The target of the inversion is to reduce the data misfit and make the model norm minimum. The objective function $\boldsymbol{\Phi}$ can be defined as

$$\boldsymbol{\Phi} = \|\boldsymbol{W}_d(\boldsymbol{d}_{obs} - \boldsymbol{F}(\boldsymbol{m}))\|^2 + \lambda\|\boldsymbol{W}_m\left(\boldsymbol{m} - \boldsymbol{m}_{ref}\right)\|^2 \tag{5}$$

where $\boldsymbol{W}_d$ is the data weight matrix, which is generally used to adjust different data weight according to the data error; $\boldsymbol{F}$ is the forward operator; $\boldsymbol{d}_{obs}$ is the observation data, which

represents measured resistance, which is equal to measured potential difference divided by measured current value; $\boldsymbol{W}_m$ is model weight matrix, which is used to model regularization in inversion; $\boldsymbol{m}$ is the logarithm of the model resistivity to ensure the resistivity is positive; $\boldsymbol{m}_{ref}$ is the reference model, which contains the prior resistivity model. In order to minimize the Equation (5), set $\partial \boldsymbol{\Phi} / \partial \Delta \boldsymbol{m} = 0$ and derive the Gauss-Newton normal equation:

$$\left(\boldsymbol{J}_k^T \boldsymbol{C}_d^{-1} \boldsymbol{J}_k + \lambda \boldsymbol{C}_m^{-1}\right) \Delta \boldsymbol{m}_k = \boldsymbol{J}_k^T \boldsymbol{C}_d^{-1} [\boldsymbol{d} - \boldsymbol{F}(\boldsymbol{m}_k)] - \lambda \boldsymbol{C}_m^{-1} \left(\boldsymbol{m}_k - \boldsymbol{m}_{ref}\right) \tag{6}$$

where $\boldsymbol{J}_k$ is the Jacobian matrix; $\boldsymbol{C}_d^{-1}$ and $\boldsymbol{C}_m^{-1}$ respectively represent the data covariance matrix and model covariance matrix, which satisfy $C_d^{-1} = \boldsymbol{W}_d^T \boldsymbol{W}_d$ and $\boldsymbol{C}_m^{-1} = \boldsymbol{W}_m^T \boldsymbol{W}_m$; $\Delta \boldsymbol{m}_k$ is the model update, which can be calculated by solving Equation (6). Finally, the model resistivity is calculated by $\boldsymbol{m}_{k+1} = \boldsymbol{m}_k + \Delta \boldsymbol{m}_k$ until the root-mean-square (RMS) misfit is minimized or reduced to the target misfit. An open-source software ResIPy [29] was used in this study. Detailed information about the simulation and inversion, such as the construction of the matrix mentioned in Equation (6), can be found in [29,34,35].

3. ERT Electrode Configurations

3.1. ERT Configurations and Sensitivity Analysis

Electrodes are the basic device for ERT measurement. They mainly have two functions. The first function is to supply electricity underground to create a current field, and the other function is to measure the voltage difference combined with other electrodes. The electrode spatial distribution of three common ERT schemes is shown in Figure 1.

The electrode configurations have a significant impact on imaging resolution. Many factors can affect the detection ability of the configurations, such as the position of current and potential electrodes, the resistivity distribution, and the data signal-to-noise ratio. Sensitivity is calculated to evaluate the detection ability of various configurations. The sensitivity of a single array can be calculated by the following Equation [36]:

$$\frac{\partial V}{\partial \rho} = \int J \cdot J' \mathrm{d}\tau \tag{7}$$

where V is the voltage between two potential electrodes; J and J' represent the current density from the point source at the transmitter and at the receiver, respectively. To test the detection capacity of ERT configurations, the configuration sensitivity of three ERT measurement schemes is shown in Figure 1. Each scheme includes one three-electrode configuration (A-MN array) and two four-electrode configurations (AB-MN array and AM-BN array). For the normalized sensitivity, the absolute value of sensitivity represents the resolution of the configurations. A high absolute sensitivity value indicates a high resolution, while low absolute sensitivity indicates a low resolution. In Figure 1a, all the electrodes are deployed on the surface. Therefore, the sensitivity of surface ERT scheme is concentrated in the region near the surface. For the BS-ERT scheme and CH-ERT scheme, the sensitivity is mainly distributed in the quadrangle made up of four electrodes, as shown in Figure 1b,c.

Typically, ERT configuration contains hundreds or thousands of measurements. Therefore, the total sensitivity distribution of different configuration is influenced by all measurements in the configuration. The total sensitivity s_j is usually calculated by the following Equation [35]:

$$s_j = \left(\boldsymbol{J}_k^T \boldsymbol{W}_d^T \boldsymbol{W}_d \boldsymbol{J}_k\right)_{jj} \tag{8}$$

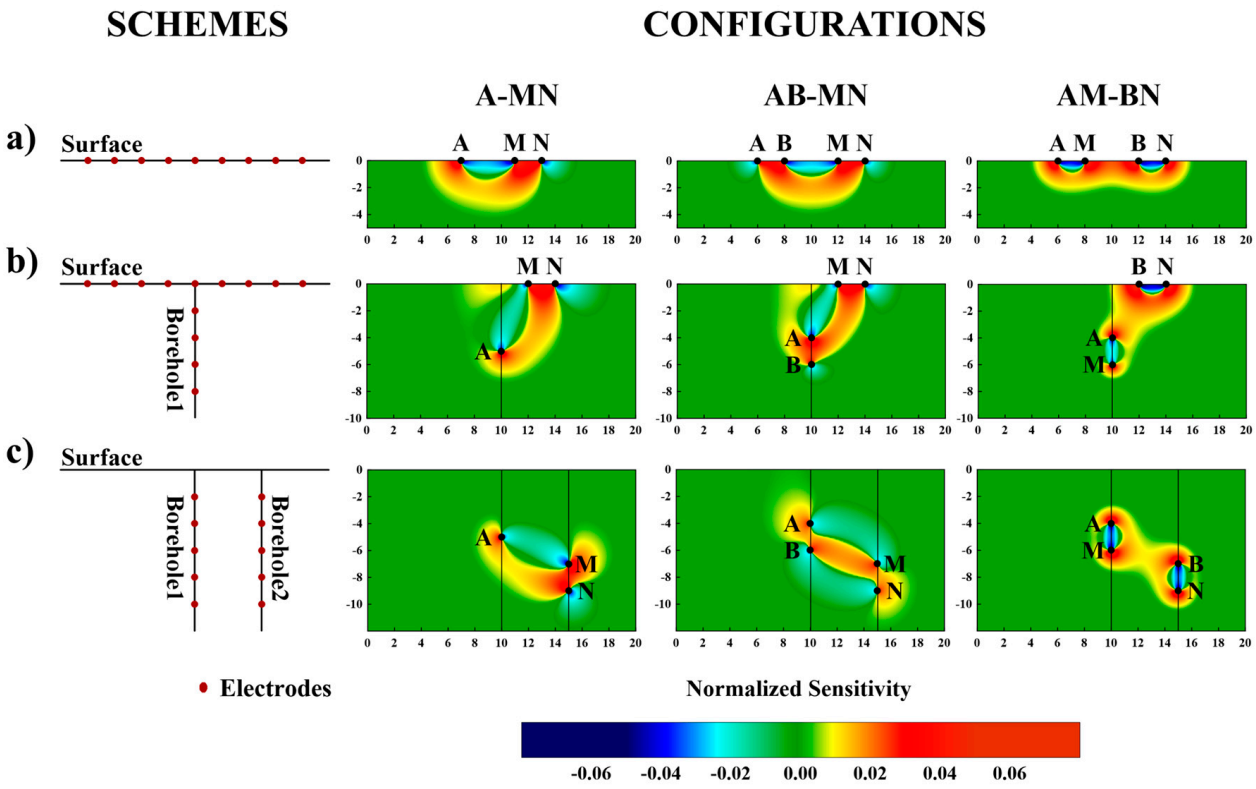

Figure 1. Electrode spatial distribution and sensitivity of three traditional ERT schemes. Row (**a**) represents the surface ERT scheme. Row (**b**) represents the BS-ERT scheme. Row (**c**) represents the CH-ERT scheme. A and B represent the positive and negative current electrodes, respectively. M and N represent the potential electrodes.

3.2. ERT Schemes for Grottoes and Sensitivity Analysis

Compared with half-space ERT schemes in Figure 1, the grotto ERT schemes are more complicated due to the existence of the cliff. The five probable grotto ERT schemes are shown in Figure 2. Among them, the surface ERT scheme and BS-ERT scheme in grotto detection, as seen in Figure 2a,b, are the same as those in half-space detection. The difference between grotto ERT schemes and half-space ERT schemes is mainly related to the schemes including cliff electrodes. The physical mechanism of cliff electrodes is identical to that of surface electrodes because both are located on the air-subsurface interface. As a result, the cliff ERT scheme in Figure 2c can use the same configurations as the surface ERT scheme with the same accuracy. The cliff electrodes are usually distributed vertically to the ground and are similar to the borehole electrodes in electrode spatial distribution because the cliffs of the grottoes are usually steep. Therefore, the configuration selections of the SC-ERT scheme and BC-ERT scheme are recommended to refer to the BS-ERT configurations and the CH-ERT configurations. In addition, the BC-ERT scheme is equivalent to the tune-to-surface ERT schemes in physical mechanism and electrode distribution [37]. Consequently, the BC-ERT scheme can also utilize the tune-to-surface ERT configurations.

The configuration sensitivity of five probable ERT measurement schemes are displayed in Figure 2. The electrode position, resistivity distribution and configurations of the relevant schemes in Figures 1 and 2 are the same in order to compare the configuration sensitivity. The comparison of the sensitivity of the surface ERT scheme and BS-ERT scheme in half-space and grotto detection (Figure 1a,b and Figure 2a,b) shows that configuration sensitivity distribute are enhanced near the top of the cliff for grotto detection. This is because the existence of the cliff obstructs the current flowing horizontally and makes the current flow along the cliff. It will improve the resolution in the region near the top of the cliff. The sensitivity distribution of near vertical-located cliff electrodes is very similar to that of borehole electrodes. The main difference is that only one side of the cliff electrodes

exists sensitivity, and the absolute value of sensitivity is improved to a certain extent compared with borehole electrodes. Therefore, for the CH-ERT scheme in Figure 1c and the BS-ERT scheme in Figure 2c, sensitivity on the left side of the cliff electrodes is improved. Additionally, the comparison of Figure 2b,d shows that the characteristics of sensitivity distribution in the SC-ERT scheme is also similar to that in the BS-ERT scheme, but mainly focused on the region between the surface and cliff.

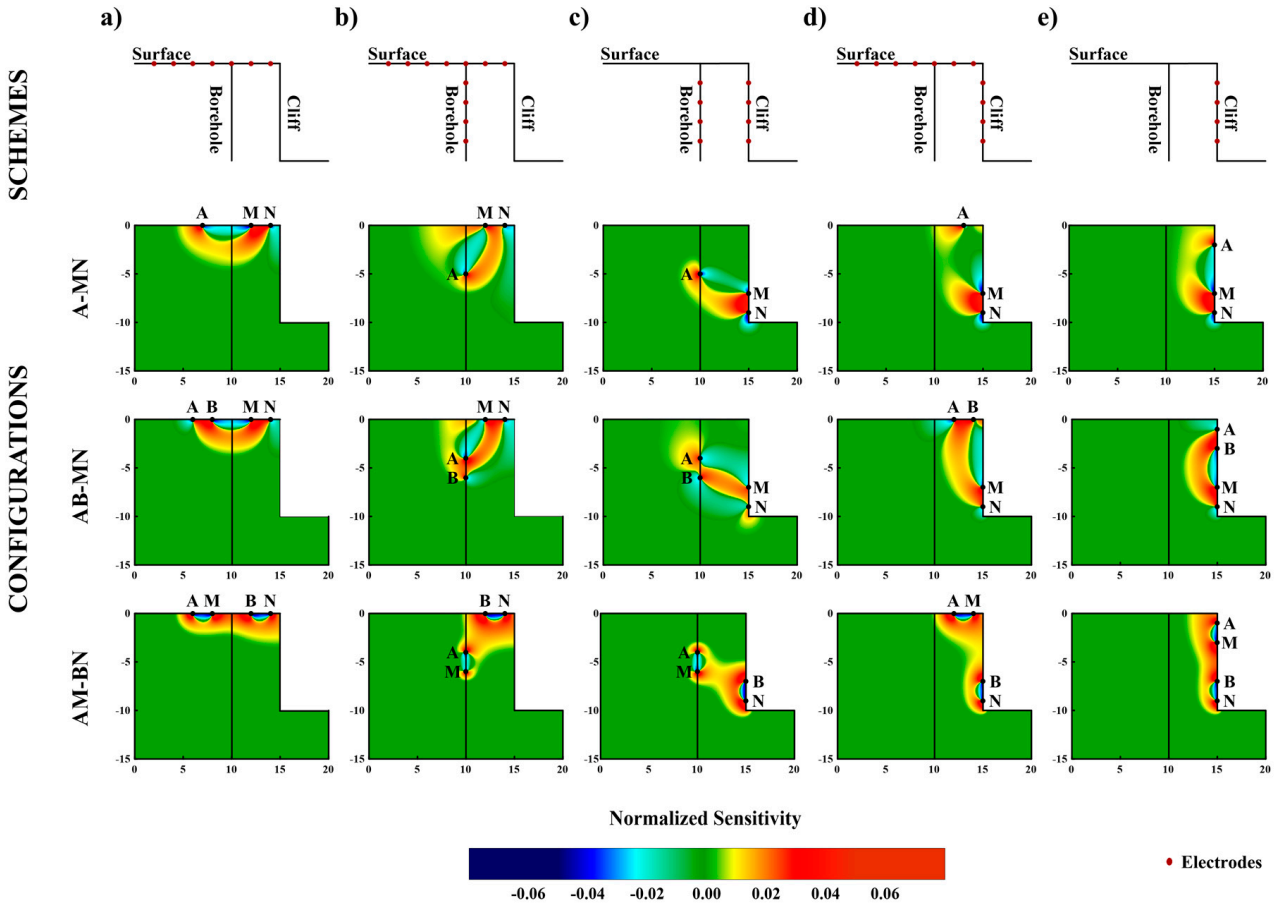

Figure 2. Electrode spatial distribution and sensitivity of five ERT schemes for grottoes. Columns (**a**–**e**) represent the surface ERT scheme, BS-ERT scheme, BC-ERT scheme, SC-ERT scheme, and cliff ERT scheme, respectively.

4. Numerical Experiments and Results

4.1. Numerical Experiment for the Block Model

A synthetic model is designed to examine and compare the imaging effect and detection capability of each configuration, as shown in Figure 3. The model consists of three layers from top to bottom. The thickness of the first two layers is 5 m and 10 m, with resistivity of 50 Ω·m and 100 Ω·m. The resistivity of the bottom layer is 150 Ω·m. There are three 5 m × 4 m blocks located in the model, and the resistivity of three blocks is 10 Ω·m and 1000 Ω·m, respectively. The data volume and the current electrode distance of each configuration in each ERT scheme is shown in Table 1.

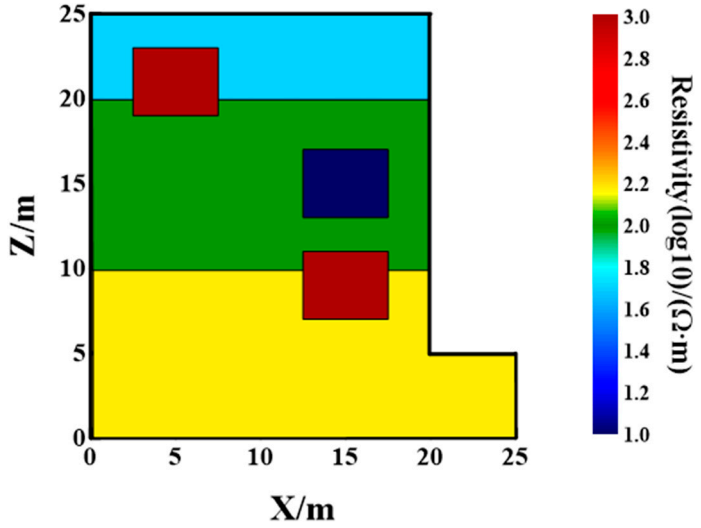

Figure 3. Synthetic model for examining and comparing numerical ERT configurations.

Table 1. The parameters of each configuration in each ERT scheme.

	Surface ERT Scheme	BS ERT Scheme	BC ERT Scheme	SC ERT Scheme	cliff ERT Scheme
A-MN array	a = 1–10 m, scanning for each electrode, Data volume: 615	a = 1–10 m, scanning for each electrode, Data volume: 2900	a = 1–10 m, scanning for each electrode, Data volume: 2900	a = 1–10 m, scanning for each electrode, Data volume: 2900	a = 1–10 m, scanning for each electrode, Data volume: 615
AB-MN array	a = 1–6 m, scanning for each electrode, Data volume: 378	a = 1–10 m, scanning for each electrode, Data volume: 2185	a = 1–10 m, scanning for each electrode, Data volume: 2185	a = 1–10 m, scanning for each electrode, Data volume: 2185	a = 1–6 m, scanning for each electrode, Data volume: 378
AM-BN array	a = 1–6 m, scanning for each electrode, Data volume: 378	a = 1–10 m, scanning for each electrode, Data volume: 2185	a = 1–10 m, scanning for each electrode, Data volume: 2185	a = 1–10 m, scanning for each electrode, Data volume: 2185	a = 1–6 m, scanning for each electrode, Data volume: 378

The sensitivity pattern and resistivity imaging are shown in Figures 4 and 5. The resolution of the region with a high sensitivity usually gets high-quality resistivity imaging. The resolution of the region, in which the logarithm of sensitivity is low, is affected by the observations and the regularization, so the anomalies of this region are difficult to image accurately. The region with a logarithm of sensitivity extremely low is the non-sensitivity region, which means this region is out of detection.

Figure 4 illustrates that the A-MN array's detection range is larger than the AB-MN and AM-BN arrays. However, most of the extra detection range belongs to the low-sensitivity region, which does not contribute much to accurate imaging. For the surface ERT scheme and cliff ERT scheme, there is less difference between the three configurations' high-resolution region. For the surface ERT scheme (Figure 5b), the AB-MN array has no capability to image the second layer for its insufficient current electrode distance. The AM-BN array has a poor recovery effect on the anomalies for the cliff ERT scheme, as illustrated in Figure 5o. Compared with the other two configurations, the A-MN array has a better imaging effect.

In Figure 5d−f, the A-MN array and the AB-MN array of the BS-ERT scheme are less effective in imaging low resistivity anomalies. In contrast, the AM-BN array has a high sensitivity and better imaging effect. Unfortunately, the AM-BN array has a symmetric effect in the BS-ERT scheme, which generates low resistivity artifacts on the left side of the borehole. In Figure 5g,h, the artifacts are also generated above the low-resistivity block when using the A-MN array and AB-MN array in the BC-ERT scheme. Furthermore,

two high-resistivity anomalies in the low-sensitivity region of the A-MN array and AB-MN array in the SC-ERT scheme are affected by the regularization effect, and the resistivity imaging is not ideal, as seen in Figure 5j,k. For the BC-ERT scheme and SC-ERT scheme, the high-resolution AM-BN array can obtain resistivity imaging without artifacts, and the imaging effect of the AM-BN array is significantly better than the other two configurations. Therefore, the AM-BN array is recommended for the BC-ERT scheme and SC-ERT scheme for its high resolution and better imaging effect.

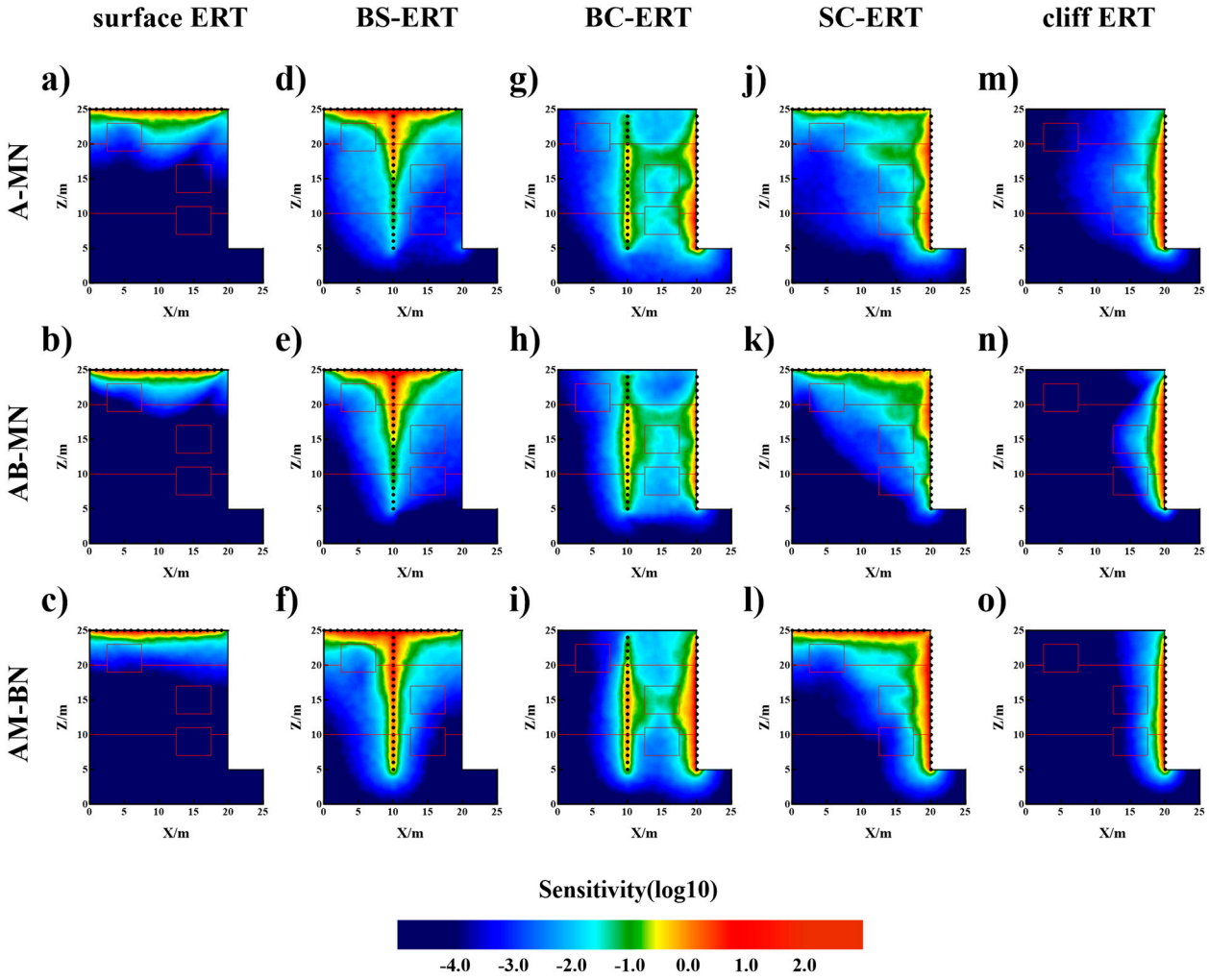

Figure 4. Sensitivity patterns of three configurations in five ERT schemes: (**a**–**c**) surface ERT scheme, (**d**–**f**) BS-ERT scheme, (**g**–**i**) BC-ERT scheme, (**j**–**l**) SC-ERT scheme, (**m**–**o**) cliff ERT scheme.

A single ERT measurement scheme is frequently insufficient for high-resolution grotto structure detection. As a result, combinations of several ERT schemes are requested in order to improve the resolution and obtain high-quality resistivity images. Four combined schemes are selected for the experiments to test the imaging effect of different combined schemes. The combined ERT scheme 1 is a combination of the surface ERT scheme and BS-ERT scheme, and it is a combination of two traditional ERT scheme. Combined scheme 2 is formed with the combination of combined scheme 1 and SC-ERT scheme, while combined scheme 3 is formed with the combination of combined scheme 1 and BC-ERT scheme. Combined scheme 4 is the scheme that contains all five probable ERT schemes.

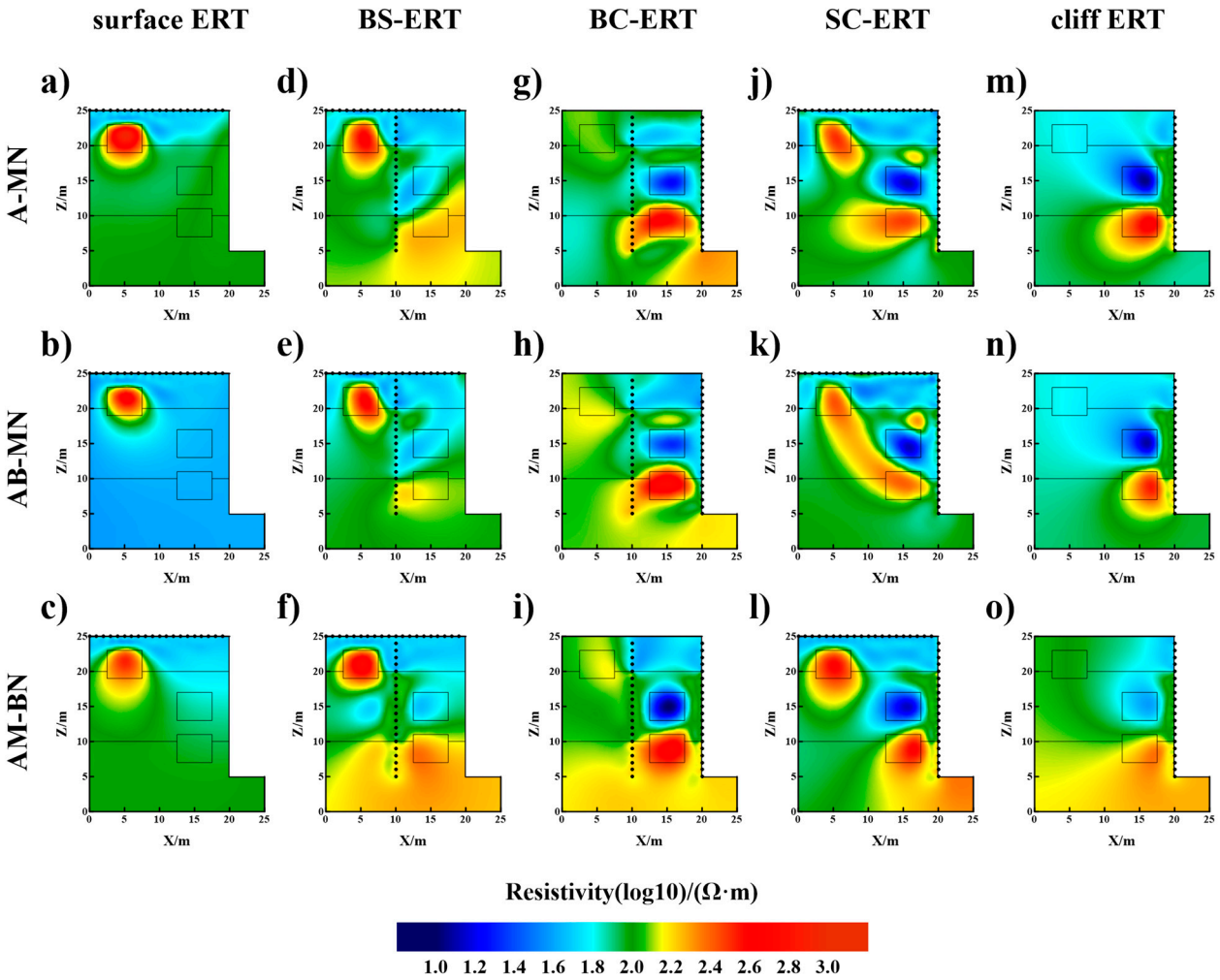

Figure 5. Resistivity imaging of three configurations in five ERT schemes: (**a**–**c**) surface ERT scheme, (**d**–**f**) BS-ERT scheme, (**g**–**i**) BC-ERT scheme, (**j**–**l**) SC-ERT scheme, (**m**–**o**) cliff ERT scheme.

Figure 6a−c and Figure 7a−c shows that the combined scheme 1 can enhance the sensitivity and improve the images of the shallow region of the BS-ERT scheme, while improves little or no imaging quality of the deeper region. The symmetric effect also exists in resistivity images in the AM-BN array, as can be seen in Figure 7c.

In combined scheme 2 and combined scheme 3, the sensitivity of the region near the cliff is improved with the data which is acquired from the schemes related to cliff electrodes, as shown in Figure 6d−i. Therefore, the region near the cliff is imaged greatly using combined schemes 2 and 3. In addition, the symmetry effect of the AM-BN array in the BS-ERT scheme is suppressed, and the artifact on the left side of the borehole disappears with the combination of SC-ERT or BC-ERT scheme, as shown in Figure 7f,i. Compared with the A-MN array and AB-MN array, the images obtained with the AM-BN array fit the experimental model better. It means that the SC-ERT scheme or BC-ERT scheme is encouraged to be implemented in fieldwork to improve the quality of inversion results.

For combined scheme 4 in Figures 6 and 7, although it has the largest amount of data and the highest sensitivity, its resistivity image is similar to that of combined schemes 2 and 3. It proves that only some of the schemes need to be implemented in grotto structure detection.

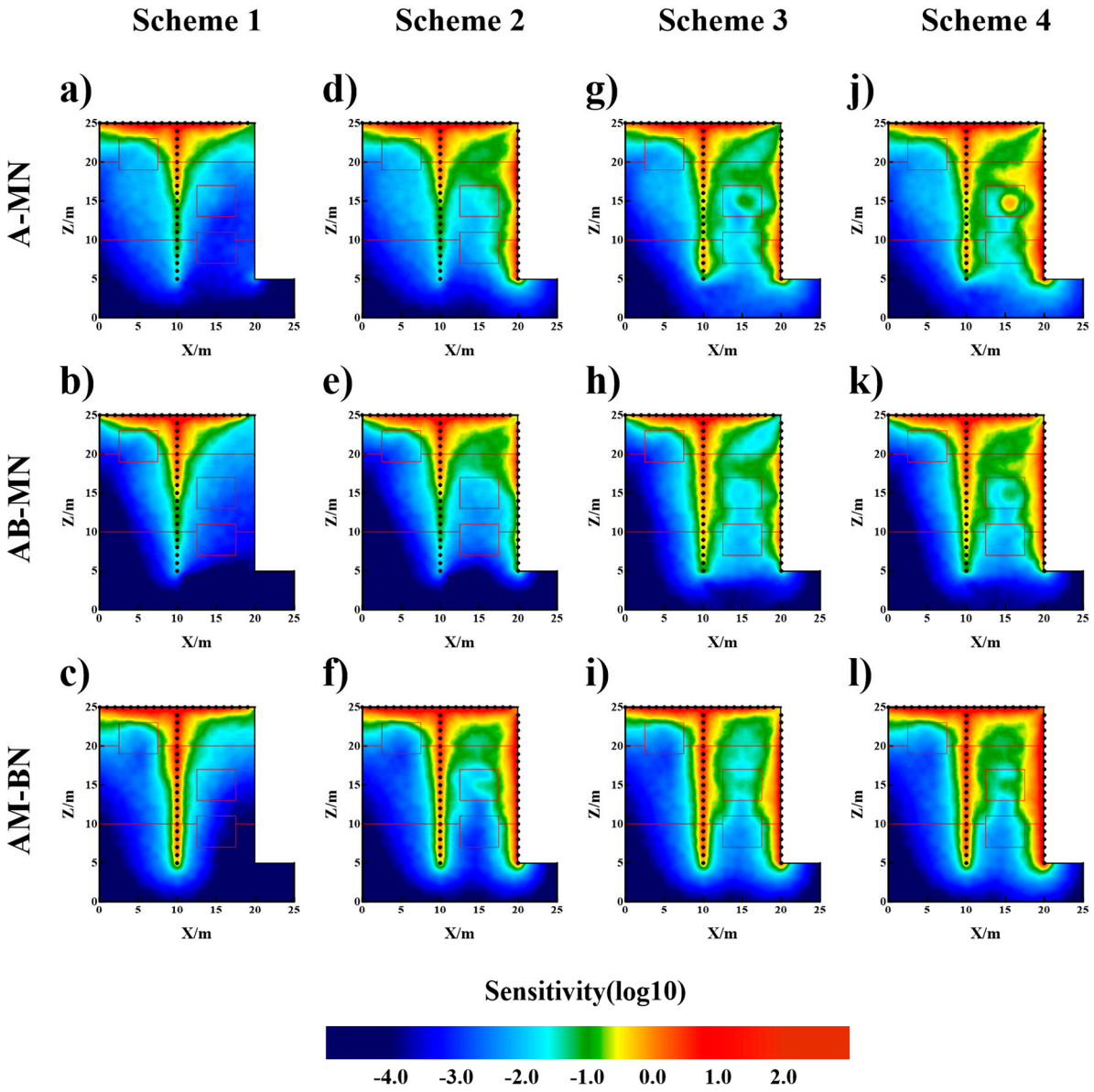

Figure 6. Sensitivity patterns for four combined schemes: (**a**–**c**) surface ERT scheme & BS-ERT scheme, (**d**–**f**) surface ERT scheme, BS-ERT scheme & SC-ERT scheme, (**g**–**i**) surface ERT scheme, BS-ERT scheme & BC-ERT scheme, (**j**–**l**) surface ERT scheme, BS-ERT scheme, SC-ERT scheme, BC-ERT scheme & cliff ERT scheme.

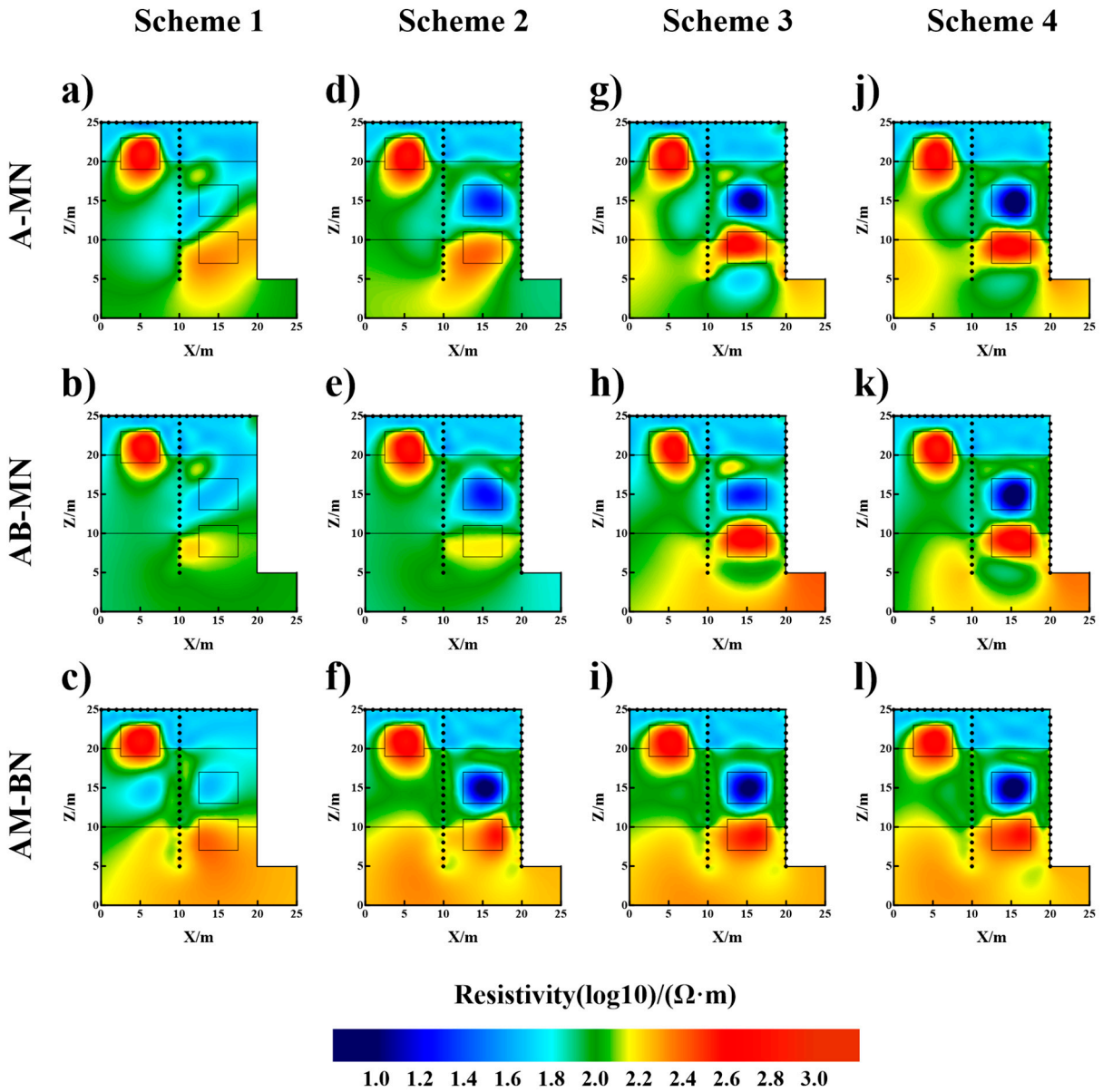

Figure 7. Resistivity images for four combined schemes: (**a**–**c**) surface ERT scheme & BS-ERT scheme, (**d**–**f**) surface ERT scheme, BS-ERT scheme & SC-ERT scheme, (**g**–**i**) surface ERT scheme, BS-ERT scheme & BC-ERT scheme, (**j**–**l**) surface ERT scheme, BS-ERT scheme, SC-ERT scheme, BC-ERT scheme & cliff ERT scheme.

4.2. Numerical Experiments for Grotto Model with Water Seepage Structure

A model with water seepage structure is established to study the best-combined schemes, which can get the best images using the least schemes, as shown in Figure 8. The resistivity of the grotto rock structure is 100 Ω·m, and the model contains three 10 Ω·m-resistivity anomalies to simulate the water seepage structure. We select the AB-MN array and AM-BN array to image this model using the BS-ERT scheme, BC-ERT scheme, and SC-ERT scheme, as shown in Figure 9a−f. This is because the detection range of the surface ERT scheme and cliff ERT scheme is not large enough to image sufficient region and the imaging effect of the A-MN array is similar to that of the AB-MN array. The parameters and data amount of three schemes are the same as those in Table 1. The combined schemes are composed of two single schemes, as shown in Figure 9g−l.

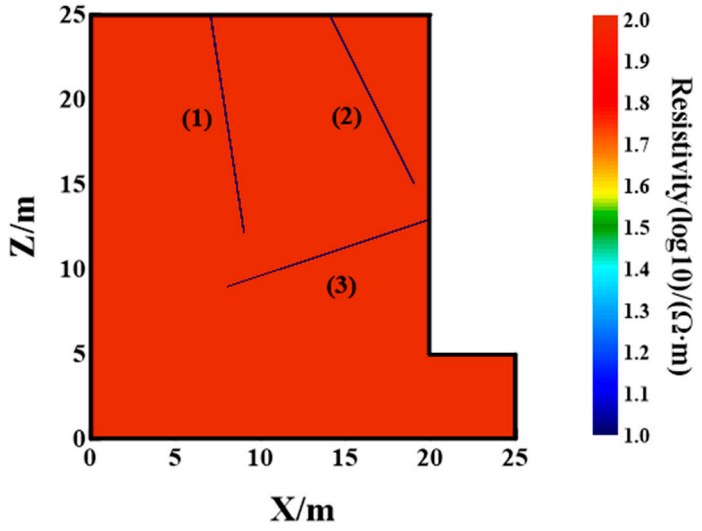

Figure 8. Grotto model with water seepage structure. (1)–(3) represent the water seepage structure. The resistivity of the grotto rock model is 100 Ω·m, the width of water seepage structure is 0.1 m, and its resistivity is 10 Ω·m.

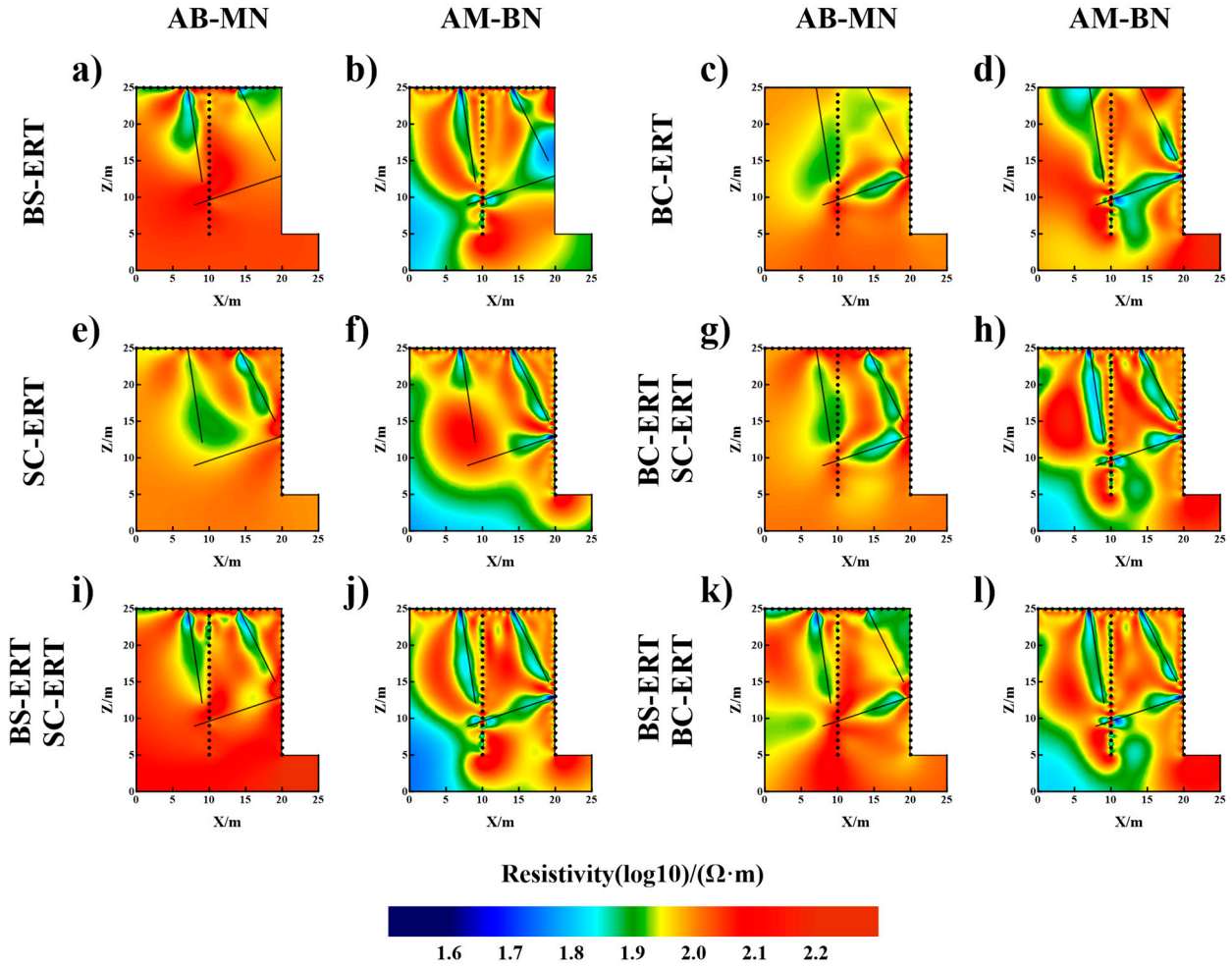

Figure 9. Resistivity images for six schemes: (**a**,**b**) BS-ERT scheme, (**c**,**d**) BC-ERT scheme, (**e**,**f**) SC-ERT scheme, (**g**,**h**) BC-ERT scheme & SC-ERT scheme, (**i**,**j**) BS-ERT scheme & SC-ERT scheme, (**k**,**l**) BS-ERT scheme & BC-ERT scheme.

The resistivity and shape of the water seepage structure is difficult to be reconstructed because of the regularization effect. However, the low-resistivity anomaly caused by the water seepage structure can still be seen from the inversion results. For single schemes, the AM-BN array is much better than the AB-MN array because some water seepage structures are hard to image using the AB-MN array, as shown in Figure 9a−f. For the BC-ERT scheme using the AM-BN array, the top of water seepage structure 2 is not imaged, and the lower part of structure 3 generates download-extending artifacts in Figure 9d. It means the detection capability of the upper and the lower regions of the AM-BN array in the BC-ERT scheme needs to be improved. Among three single schemes using the AM-BN array, the resistivity image of the SC-ERT scheme is the best for its high resolution.

For combined schemes using the AM-BN array, the artifacts generated in the BC-ERT scheme also appear in the combined scheme, as shown in Figure 9d,h,l. Comparing the inversion results in Figure 9, it is found that the resistivity imaging of the combination of the BS-ERT scheme and SC-ERT scheme is not too much affected by the low-resistivity artifacts and is the best of three combined schemes.

5. Discussion

At present, the surface ERT and BS-ERT scheme are commonly used in grotto structure detection. However, there are some shortcomings in these two schemes. Numerical experiments show that the depth of the surface ERT scheme is shallow, and the resolution of the BS-ERT scheme or combined scheme 1 in Figures 5 and 7 needs to be revised in the region far from the surface and the borehole. Therefore, these schemes have limited capability to detect the cliff, which is the key region we are concerned about and needs to be detected accurately. Moreover, the high-resolution AM-BN array of the BS-ERT scheme is easily affected by the symmetric effect and generates artifacts, which brings a great interface to the later interpretation.

In this situation, we propose the BSC-ERT scheme based on the BS-ERT scheme. Grottoes are usually carved into layered sandstone, which can be approximated as a 2D structure. 2D measurement schemes can solve the practical problem well with lower cost, higher measurement efficiency, and computing efficiency than 3D measurement schemes. The new proposed scheme has two advantages. The first advantage is that the BSC-ERT scheme not only inherits both surface ERT and BS-ERT scheme, but also has more SC-ERT scheme, BC-ERT scheme, and cliff ERT scheme due to the deployment of cliff electrodes. These three schemes can provide better images of the region near the cliff. Among them, the AM-BN array of SC-ERT scheme has a high resolution on the region near the surface and cliff, where we are more concerned and can obtain high-quality image. The second advantage is that the symmetric effect of the AM-BN array in the BS-ERT scheme can be avoided by combining the BS-ERT scheme with BC-ERT or SC-ERT scheme. This finding might lead to a new way to solve the symmetric effect of the AM-BN array. The BC-ERT scheme can significantly increase the sensitivity of the right side of the borehole while the sensitivity of the left side of the borehole is slightly increased. This kind of the increasement is not symmetric. The same is true of the SC-ERT scheme. Combining the asymmetric measurement scheme with the BS-ERT scheme is very likely to suppress its symmetric effect, which is important for high-resolution imaging for the BS-ERT scheme.

The other finding is that not all five schemes need to be implemented to obtain an acceptable resistivity image. The comparison of resistivity images for a single scheme shows that the schemes with surface electrodes and cliff electrodes are more stable and have fewer artifacts than the schemes with borehole electrodes, as shown in Figure 9a−f. Therefore, the SC-ERT scheme using the AM-BN array is the most recommended scheme to be implemented in grotto structure detection. The BS-ERT scheme can be used to improve the detection capability of the region away from the cliff and the surface combined with the SC-ERT scheme, as shown in Figures 7 and 9.

How to apply the BSC-ERT scheme in field experiments will be discussed in this section. Traditional surface ERT scheme and BS-ERT scheme can be measured in a general

way. For the schemes with cliff electrodes, a new type of cliff electrodes similar to electrocardiograph electrodes should be developed to replace the traditional copper electrodes. It should be able to be attached to the cliff and meet the voltage requirement for the measurement. The research and development of electrodes is of great significance and can not only be used for grotto structure detection, which can make ERT applied to more study sites, such as ancient walls, vertical dam, and tunnel walls. Field research will be carried out in the future after the development of the cliff electrodes. In addition, although numerical simulation and inversion about vertical cliff are studied in this research, the results are still instructive for models with very steep slopes.

6. Conclusions

In this paper, we proposed a new ERT scheme, called the BSC-ERT scheme, based on the BS-ERT scheme for grotto structure detection. Through the study of numerical experiments, it is confirmed that traditional surface ERT and BS-ERT scheme have a weak ability to detect the region near the cliff. It is essential to deploy cliff electrodes to improve imaging effects. The new proposed scheme not only inherits all the advantages of the BS-ERT scheme, but also improves the resolution of the region we are concerned about. The numerical experiments also indicate that the AM-BN array of the combination of BS-ERT and SC-ERT scheme is recommended to get acceptable resistivity images, which have high resolution on the anomalies and generate the least artifacts. The study of the BSC-ERT scheme will provide theoretical guidance for field experiments in the future and avoid unnecessary workload.

Meanwhile, the experiments of combined schemes provide a new solution to suppress the symmetric effect of the AM-BN array in BS-ERT scheme. Artifacts caused by symmetric effects can be eliminated by combining an asymmetric scheme, such as SC-ERT or BC-ERT scheme, with the BS-ERT scheme. Although this conclusion is summarized for the grotto measurement scheme, it is still instructive for the combined scheme for BS-ERT and CH-ERT scheme.

Author Contributions: Conceptualization, Z.Z., J.L. and J.Y.; methodology, J.Y. and Z.Z.; software, J.Y.; validation, J.Y. and J.Z.; formal analysis, Z.Z. and J.Y.; investigation, J.Y. and L.B.; resources, J.Y. and B.A.; data curation, J.Y.; writing—original draft preparation, J.Y.; writing—review and editing, Z.Z., X.Z., J.L. and J.Y.; visualization, J.Y.; supervision, Z.Z. and J.L.; project administration, J.L. and Z.Z.; funding acquisition, J.L., Z.Z. and B.A. All authors have read and agreed to the published version of the manuscript.

Funding: This research was funded by National Key Research and Development Program of China (grant number: 2021YFC1523401) and Ningxia Hui Autonomous Region's 2022 Science and Technology Benefiting the People Project (grant number: 2022CMG03006).

Data Availability Statement: Not applicable.

Acknowledgments: The authors would like to thank the editors and reviewers for providing their valuable comments and suggestions.

Conflicts of Interest: The authors declare no conflict of interest.

References

1. Liu, Q.X.; Duan, Y.H.; Deng, J.Y. Geological Protection Project of the Longmen Grottoes in Luoyang. *Adv. Mater. Res.* **2012**, *155*, 594–597. [CrossRef]
2. Qu, J.; Cao, S.; Li, G.; Niu, Q.; Feng, Q. Conservation of natural and cultural heritage in Dunhuang, China. *Gondwana Res.* **2014**, *26*, 1216–1221. [CrossRef]
3. Zhou, S.W.; Xia, C.C.; Huang, M. Long-term stability of rock pillars in the Longyou Ancient Grottoes: Sonic wave detection and numerical investigation. *Anc. Undergr. Open. Preserv.* **2016**, 395–400.
4. Wang, X.D.; Wang, Y.W.; Guo, Q.L.; Pei, Q.Q.; Zhao, G.J. The history of rescuing reinforcement and the preliminary study of preventive protection system for the cliff of Mogao Grottoes in Dunhuang, China. *Herit. Sci.* **2021**, *9*, 58. [CrossRef]
5. Kai, L.; Li, Z.Y.; Niu, R.Q.; Fan, L.; Pan, J.W.; Li, K.T.; Liang, C. Using surface nuclear magnetic resonance and spontaneous potential to investigate the source of water seepage in the JinDeng Temple grottoes, China. *J. Cult. Herit.* **2020**, *45*, 142–151.

6. Wanfu, W. Detection of Delamination in Wall Paintings by Ground Penetrating Radar. In *Behaviour of Electromagnetic Waves in Different Media and Structures*; Ali, A., Ed.; IntechOpen: Rijeka, Croatia, 2011; p. 7.
7. Joshi, M.; Prasobh, P.R.; Rajappan, S.; Rao, B.P.; Gond, A.; Misra, A.; Eldhose, K.; Nandakumar, V.; Tomson, J.K. Detection of soil pipes through remote sensing and electrical resistivity method: Insight from southern Western Ghats, India. *Quatern Int.* **2021**, *575*, 51–61. [CrossRef]
8. Joshi, M.; Gond, A.; Prasobh, P.R.; Rajappan, S.; Padma Rao, B.; Nandakumar, V. Chapter 5—Significance and limit of electrical resistivity survey for detection sub surface cavity: A case study from, Southern Western Ghats, India. In *Basics of Computational Geophysics*; Samui, P., Dixon, B., Tien Bui, D., Eds.; Elsevier: Amsterdam, The Netherlands, 2021; pp. 81–93.
9. Dahlin, T.; Zhou, B. A numerical comparison of 2D resistivity imaging with 10 electrode arrays. *Geophys. Prospect.* **2004**, *52*, 379–398. [CrossRef]
10. Zhou, B.; Bouzidi, Y.; Ullah, S.; Asim, M. A full-range gradient survey for 2D electrical resistivity tomography. *Near Surf. Geophys.* **2020**, *18*, 609–626. [CrossRef]
11. Tsourlos, P.; Ogilvy, R.; Papazachos, C.; Meldrum, P. Measurement and inversion schemes for single borehole-to-surface electrical resistivity tomography surveys. *J. Geophys. Eng.* **2011**, *8*, 487–497. [CrossRef]
12. Goes, B.J.M.; Meekes, J.A.C. An effective electrode configuration for the detection of DNAPLs with electrical resistivity tomography. *J. Environ. Eng. Geoph.* **2004**, *9*, 127–141. [CrossRef]
13. Wang, H.R.; Lin, C.P. Cause and countermeasures for the symmetric effect in borehole-to-surface electrical resistivity tomography. *J. Appl. Geophys.* **2018**, *159*, 248–259. [CrossRef]
14. LaBrecque, D.J.; Ramirez, A.L.; Daily, W.D.; Binley, A.M.; Schima, S.A. ERT monitoring of environmental remediation processes. *Meas. Sci. Technol.* **1996**, *7*, 375–383. [CrossRef]
15. Wang, H.R.; Lin, C.P.; Mok, T.H.; Wu, P.L.; Liu, H.C. High-fidelity subsurface resistivity imaging incorporating borehole measurements for monitoring underground construction. *Eng. Geol.* **2022**, *299*, 106558. [CrossRef]
16. McCormack, T.; O'Connell, Y.; Daly, E.; Gill, L.W.; Henry, T.; Perriquet, M. Characterisation of karst hydrogeology in Western Ireland using geophysical and hydraulic modelling techniques. *J. Hydrol.-Reg. Stud.* **2017**, *10*, 1–17. [CrossRef]
17. Tejero-Andrade, A.; Argote-Espino, D.L.; Cifuentes-Nava, G.; Hernandez-Quintero, E.; Chavez, R.E.; Garcia-Serrano, A. 'Illuminating' the interior of Kukulkan's Pyramid, Chichen Itza, Mexico, by means of a non-conventional ERT geophysical survey. *J. Archaeol. Sci.* **2018**, *90*, 1–11. [CrossRef]
18. Imani, P.; Tian, G.; Hadiloo, S.; Abd El-Raouf, A. Application of combined electrical resistivity tomography (ERT) and seismic refraction tomography (SRT) methods to investigate Xiaoshan District landslide site: Hangzhou, China. *J. Appl. Geophys.* **2021**, *184*, 104236. [CrossRef]
19. Guo, Y.J.; Cui, Y.A.; Xie, J.; Luo, Y.J.; Zhang, P.F.; Liu, H.F.; Liu, J.X. Seepage detection in earth-filled dam from self-potential and electrical resistivity tomography. *Eng. Geol.* **2022**, *306*, 106750. [CrossRef]
20. Su, M.X.; Liu, Y.M.; Li, H.Y.; Li, C.C.; Wang, P.; Ma, X.Y. Water Inrush Detection in Limestone Pit Rock Walls Using Borehole-to-Surface ERT. *Mine Water Environ.* **2021**, *40*, 1061–1072. [CrossRef]
21. Leontarakis, K.; Apostolopoulos, G.V. Model Stacking (MOST) technique applied in cross-hole ERT field data for the detection of Thessaloniki ancient walls' depth. *J. Appl. Geophys.* **2013**, *93*, 101–113. [CrossRef]
22. Li, N.B.; Dong, Z.; Liu, Z.Y.; Yan, B.; Wang, K.; Nie, L.C.; Lin, C.J.; Shen, J.F.; Ma, Z.; Zhang, Y.H. Synthetic Study of Boulder Detection Using Multi-Configuration Combination of Cross-Hole ERT and Its Field Application in Xiamen Metro, China. *Appl. Sci.* **2021**, *11*, 11860. [CrossRef]
23. Huang, J.Z.; Ren, J.G. Geophysical prospecting method applied in the preservation of Yungang Grottoes. *Sci. Conserv. Archaeol.* **2011**, *23*, 87–95. (In Chinese)
24. Fang, Y.; Qiao, L.; Yan, X.F.; Chen, H.L.; Liu, J.P. The application of geophysical technology in the conservation of Dazu rock cavings. *Geophys. Geochem. Explor.* **2013**, *37*, 138–142. (In Chinese)
25. Keigo, K.; Kazuhiro, O.; Misae, I.; Piao, C.Z.; Chikaosa, T.; Yoshinori, I.; Mitsugu, Y.; Wang, X.D.; Guo, Q.L.; Yang, S.L. Estimation of Hydraulic Environment behind the Mogao Grottoes Based on Geophysical Explorations and Laboratory Experiment. *Eng. Geol. Soc. Territ. Preserv. Cult. Herit.* **2015**, *8*, 71–74.
26. Sun, M.; Zhang, J.; Zhang, L.; Wang, X.; Guo, Q.; Pei, Q.; Wang, Y. Multi-electrode resistivity survey for the moisture distribution characteristics of the cliff of Mogao Grottoes. *Bull. Eng. Geol. Environ.* **2022**, *81*, 489. [CrossRef]
27. Liu, H.L.; Wang, X.D.; Guo, Q.L.; Zhang, M.Q.; Wang, Y.W. Experimental investigation on the correlation between rainfall infiltration and the deterioration of wall paintings at Mogao Grottoes, China. *B Eng. Geol. Environ.* **2020**, *79*, 1199–1207. [CrossRef]
28. Mao, D.Q.; Wang, X.D.; Meng, J.; Ma, X.M.; Jiang, X.W.; Wan, L.; Yan, H.B.; Fan, Y. Infiltration Assessments on Top of Yungang Grottoes by Time-Lapse Electrical Resistivity Tomography. *Hydrology* **2022**, *9*, 77. [CrossRef]
29. Blanchy, G.; Saneiyan, S.; Boyd, J.; McLachlan, P.; Binley, A. ResIPy, an intuitive open source software for complex geoelectrical inversion/modeling. *Comput. Geosci.* **2020**, *137*, 104423. [CrossRef]
30. LaBrecque, D.J.; Miletto, M.; Daily, W.; Ramirez, A.; Owen, E. The effects of noise on Occam's inversion of resistivity tomography data. *Geophysics* **1996**, *61*, 538–548. [CrossRef]
31. Xu, S.Z.; Duan, B.C.; Zhang, D.H. Selection of the wavenumbers k using an optimization method for the inverse Fourier transform in 2.5D electrical modelling. *Geophys. Prospect.* **2000**, *48*, 789–796. [CrossRef]

32. Kemna, A. Tomographic Inversion of Complex Resistivity-Theory and Application. Ph.D. Dissertation, Ruhr-University of Bochum, Bochum, Germany, 2000.
33. Karaoulis, M.; Revil, A.; Tsourlos, P.; Werkema, D.D.; Minsley, B.J. IP4DI: A software for time-lapse 2D/3D DC-resistivity and induced polarization tomography. *Comput. Geosci.* **2013**, *54*, 164–170. [CrossRef]
34. Binley, A. Tools and Techniques: Electrical Methods. In *Treatise on Geophysics*; Schubert, G., Ed.; Elsevier: Oxford, UK, 2015; pp. 233–259.
35. Binley, A.; Kemna, A. DC Resistivity and Induced Polarization Methods. In *Hydrogeophysics*; Rubin, Y., Hubbard, S.S., Eds.; Springer: Dordrecht, The Netherlands, 2005; pp. 129–156.
36. Park, S.K.; Van, G.P. Inversion of pole-pole data for 3-D resistivity structure beneath arrays of electrodes. *Geophysics* **1991**, *56*, 951–960. [CrossRef]
37. Tsokas, G.N.; Tsourlos, P.I.; Kim, J.H.; Papazachos, C.B.; Vargemezis, G.; Bogiatzis, P. Assessing the Condition of the Rock Mass over the Tunnel of Eupalinus in Samos (Greece) using both Conventional Geophysical Methods and Surface to Tunnel Electrical Resistivity Tomography. *Archaeol. Prospect* **2014**, *21*, 277–291. [CrossRef]